

Model-independent evidence in favor of an end to reionization by $z \approx 6$

Ian D. McGreer,^{1,*} Andrei Mesinger,² and Valentina D’Odorico³

¹ *Steward Observatory, The University of Arizona, 933 North Cherry Avenue, Tucson, AZ 85721-0065*

² *Scuola Normale Superiore, Piazza dei Cavalieri 7, I-56126 Pisa, Italy*

³ *INAF-OATS, Via Tiepolo 11, I-34143 Trieste, Italy*

22 August 2018

ABSTRACT

We present new upper limits on the volume-weighted neutral hydrogen fraction, \bar{x}_{HI} , at $z \sim 5\text{--}6$ derived from spectroscopy of bright quasars. The fraction of the Ly α and Ly β forests that is “dark” (with zero flux) provides the only model-independent upper limit on \bar{x}_{HI} , requiring no assumptions about the physical conditions in the intergalactic medium or the quasar’s unabsorbed UV continuum. In this work we update our previous results using a larger sample (22 objects) of medium-depth (\sim few hours) spectra of high-redshift quasars obtained with the Magellan, MMT, and VLT. This significantly improves the upper bound on \bar{x}_{HI} derived from dark pixel analysis to $\bar{x}_{\text{HI}} \leq 0.06+0.05$ (1σ) at $z = 5.9$ and $\bar{x}_{\text{HI}} \leq 0.04+0.05$ (1σ) at $z = 5.6$. These results provide robust constraints for theoretical models of reionization, and provide the strongest available evidence that reionization has completed (or is very nearly complete) by $z \approx 6$.

Key words: Galaxies: high-redshift – Cosmology: observations – dark ages, reionization, first stars – diffuse radiation – early Universe – quasars: absorption lines

1 INTRODUCTION

Cosmic reionization was the last major phase change of the baryons in our Universe. The state of the intergalactic medium (IGM) during this epoch provides unique insight into the nature of the first structures. Thus observational probes of reionization have been long sought-after. The first suggestive evidence of reionization came from the rapid redshift evolution of observed flux in the Ly α and Ly β forests of $z \sim 6$ QSO spectra (e.g. Fan et al. 2001; White et al. 2003). Subsequent reionization studies have exploited: (i) the size and evolution of the proximity zone around quasars (e.g. Wyithe et al. 2005; Fan et al. 2006; Carilli et al. 2010; Bolton & Haehnelt 2007; Maselli et al. 2007); (ii) the damping wing absorption from neutral IGM in quasar and gamma-ray burst spectra (e.g. Mesinger & Haiman 2004; Totani et al. 2006; Mesinger & Haiman 2007; McQuinn et al. 2008; Bolton et al. 2011; Schroeder et al. 2012; Totani et al. 2013); (iii) the number density and clustering of Ly α emitters (e.g. Malhotra & Rhoads 2004; Kashikawa et al. 2006; McQuinn et al. 2007; Dijkstra et al. 2011; Dayal et al. 2011; Jensen et al. 2013; Konno et al. 2014; Mesinger et al. 2014); (iv) the distribution of dark gaps in quasar spectra (e.g. Croft

1998; Songaila & Cowie 2002; Gallerani et al. 2006, 2008; Mesinger 2010); (v) the integral constraints provided by the CMB primary (e.g. Hinshaw et al. 2013) and secondary (e.g. Zahn et al. 2012; Mesinger et al. 2012) anisotropies.

Despite these efforts, no consensus has emerged as to whether or not we are witnessing the epoch of reionization at $z \sim 6$. The many uncertainties and degeneracies inherent in modeling high-redshift astrophysics complicate the interpretation of the observational data. This problem is exacerbated by the expectation that reionization is very inhomogeneous on large-scales (e.g. Furlanetto et al. 2004; Zahn et al. 2011). As such, the statistics available today are too limited to provide robust constraints; thus it is not even certain that reionization has completed by $z \lesssim 6$, as cosmic neutral patches of the IGM could easily masquerade as saturated regions of the Ly α forest (Lidz et al. 2007; Mesinger 2010).

In a previous work (McGreer et al. 2011, hereafter Paper I), we examined the Ly α and Ly β forests of high-redshift quasars with spectra from the ESI instrument on the Keck II telescope. After binning the spectra to increase the dynamic range, we measured the fraction of binned pixels that were dark in both forests (the so-called “dark fraction”; Mesinger 2010). Using just two high signal-to-noise (S/N) spectra with ~ 10 hr integration times, we constrained the volume-

* Email: imcgreer@as.arizona.edu

weighted mean neutral fraction of the IGM at $z \approx 5.9$ to be $\bar{x}_{\text{HI}} \lesssim 0.3$ (1σ). The dark fraction is only an upper limit on \bar{x}_{HI} , as the residual H I inside the ionized IGM can also be sufficient to saturate Ly α and Ly β at these redshifts (i.e. the dark patches need not correspond to cosmic H I regions during patchy reionization). Nevertheless, our upper limits are competitive, and more importantly, are *the only model-independent limits on \bar{x}_{HI} to date*.

In this work we update our results from Paper I. We apply the same analysis on a much larger sample of $z \sim 6$ quasar spectra having total integration times of several hours on 6-10m class telescopes. We present the new observations from Magellan, MMT, and the VLT in §2, then summarize the dark pixel analysis of the new spectra in §3. The result is a much stronger upper limit on the neutral hydrogen fraction at $z < 6$ as detailed in §4. We adopt a Λ CDM cosmology with identical parameters as in Paper I: $(\Omega_{\Lambda}, \Omega_{\text{M}}, H_0) = (0.72, 0.28, 70 \text{ km s}^{-1} \text{ Mpc}^{-1})$; Komatsu et al. 2009); this is required only to convert redshift bins to comoving distances and thus our results have negligible dependence on the choice of cosmological model.

2 DATA

In Paper I we presented results derived from 13 spectra obtained with the ESI instrument on the Keck II telescope. With the exception of two deep (~ 10 hr) spectra, the data came from shallow (≤ 1 hr) observations. We include the original ESI sample in the analysis presented here, but add new, deeper observations of $z \sim 6$ quasars obtained with moderate resolution spectrographs on the Magellan, MMT, and VLT telescopes. The complete list of spectra is given in Table 1; the following sections describe the new observations.

2.1 Magellan Spectra

We observed four quasars at the Magellan Clay 6.5m on 2011 Jun 10-13 using the Magellan Echellette spectrograph (MagE; Marshall et al. 2008). MagE combines a grating with two cross-dispersing prisms to project 15 spectral orders onto a 2048×1024 E2V CCD, providing wavelength coverage from 3000\AA to $1.05\mu\text{m}$. We employed the $0.7'' \times 10''$ slit, yielding a resolution of $R \sim 5800$. The native dispersion varies from $0.3 \text{ \AA pixel}^{-1}$ at the blue end to $0.6 \text{ \AA pixel}^{-1}$ at the red end. Conditions were generally clear and non-photometric, with seeing ranging from $0''.6$ – $0''.8$.

The Magellan spectra were processed with MASE (Bochanski et al. 2009), an IDL-based pipeline designed for MagE data. The calibration procedures outlined in Bochanski et al. (2009) were followed. In brief, wavelength calibration is obtained from thorium-argon arcs observed immediately after the science targets. The pixel flat-field images, slit illumination corrections, and the order traces are obtained from a combination of internal lamps and sky flats. The spectrophotometric standard star Feige 110 was observed each night to provide flux calibration. With the exception of J1420-1602, spectra for each target were obtained over multiple nights. The spectra for each night were processed separately and then scaled and combined with inverse-variance

Table 1. Quasar spectra

| Object | z | z_{AB} | t_{exp} | $\langle \tau_{\text{eff,lim}}^{\alpha} \rangle$ | source |
|------------|------|-----------------|------------------|--|----------|
| J1420-1602 | 5.73 | 19.7 | 4.00 | 5.3 | MagE |
| J0927+2001 | 5.77 | 19.9 | 0.33 | 3.8 | ESI |
| J1044-0125 | 5.78 | 19.2 | 4.79 | 5.2 | MagE |
| J0836+0054 | 5.81 | 18.7 | 0.33 | 4.7 | ESI |
| | | | 4.00 | 3.9 | MMT |
| | | | 2.27 | 5.9 | XShooter |
| J0002+2550 | 5.82 | 19.0 | 2.76 | 3.6 | MMT |
| J0840+5624 | 5.84 | 19.8 | 0.33 | 4.1 | ESI |
| J1335+3533 | 5.90 | 20.1 | 0.33 | 3.8 | ESI |
| J1411+1217 | 5.90 | 19.6 | 1.00 | 3.7 | ESI |
| J0148+0600 | 5.92 | 19.4 | 10.00 | 6.3 | XShooter |
| J0841+2905 | 5.98 | 19.8 | 0.33 | 3.5 | ESI |
| J1306+0356 | 6.02 | 19.5 | 0.25 | 4.3 | ESI |
| | | | 11.50 | 5.4 | XShooter |
| J0818+1722 | 6.02 | 19.6 | 4.50 | 4.6 | MMT |
| | | | 5.90 | 5.7 | XShooter |
| J1137+3549 | 6.03 | 19.5 | 0.67 | 3.8 | ESI |
| | | | 2.33 | 3.7 | MMT |
| J2054-0005 | 6.04 | 20.7 | 11.00 | 4.4 | MagE |
| J0353+0104 | 6.05 | 20.5 | 1.00 | 3.5 | ESI |
| J1630+4012 | 6.07 | 20.4 | 4.39 | 3.2 | MMT |
| J0842+1218 | 6.08 | 19.6 | 0.67 | 4.0 | ESI |
| J1509-1749 | 6.12 | 20.3 | 6.00 | 4.7 | MagE |
| | | | 8.32 | 5.2 | XShooter |
| J1319+0950 | 6.13 | 20.0 | 10.00 | 5.7 | XShooter |
| J1623+3112 | 6.25 | 20.1 | 1.00 | 4.2 | ESI |
| J1030+0524 | 6.31 | 20.0 | 10.32 | 5.3 | ESI |
| | | | 7.46 | 5.4 | XShooter |
| J1148+5251 | 6.42 | 20.1 | 11.00 | 6.0 | ESI |

Notes: Exposure times are given in hours. $\langle \tau_{\text{eff,lim}}^{\alpha} \rangle$ is the median effective optical depth in the Ly α forest for a pixel (binned to 3.3 cMpc) with a flux equivalent to the 1σ noise estimate.

weighting using the MASE routine LONG_COMBSPEC. The variance does not include an estimate for the Poisson contribution due to the object flux, as this would bias the result in low-count regions (see discussion in White et al. 2003). The final spectra are displayed in Figure 1.

The MagE data from the first three nights are affected by increased and variable readnoise. The nominal readnoise is $3.1 e^-$, which agrees with measurements taken after the problem was addressed. Analysis of the overscan regions shows that the readnoise varied from ~ 5 – $7 e^-$ in images from the first ~ 2.5 nights of observations. The dark pixel analysis we perform is concentrated on regions with low sky background between the strong night sky emission lines; hence the augmented readnoise diminishes the sensitivity of the spectra and has the effect of reducing the effective exposure time. We include readnoise estimates from the overscan regions in the variance calculation used by MASE in order to account for this issue.

2.2 MMT Spectra

Spectroscopy of five quasars was performed with the Red Channel spectrograph on the MMT 6.5m telescope during the nights of 2011 Jan 3-4 (J0836+0054, J0818+1722, and J1137+3549) and 2011 Jul 4-6 (J1630+4012 and J0002+2550). The Red Channel instrument includes an

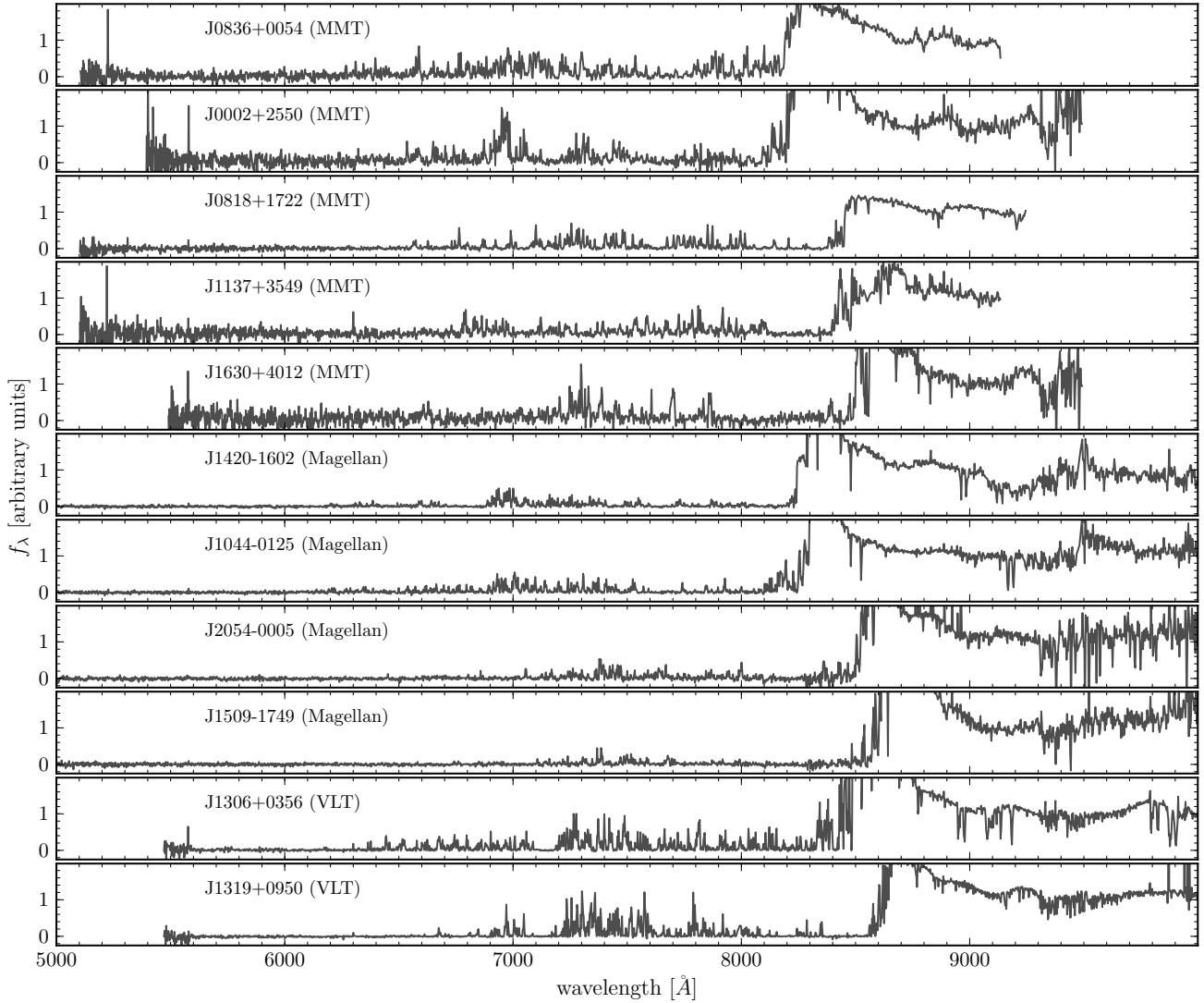


Figure 1. Spectra of $z \sim 6$ quasars used for the dark pixel analysis. Further details for each spectrum are given in Table 1. The spectra have been rebinned to a dispersion of $\sim 2.5 \text{ \AA pix}^{-1}$ for clarity, and normalized by their flux density at rest-frame $\sim 1350 \text{ \AA}$; the displayed scale is arbitrary but the same in each panel. The transmission spikes become sharper as the resolution increases from the MMT to Magellan to VLT data.

echellette mode that combines a grating with a single cross-disperser to provide complete coverage over a wavelength range of $\sim 4000 \text{ \AA}$. We set the blaze angle of the grating to its nominal value of 4.555 and the cross-disperser at 350 (340 for the June observations). These settings project roughly nine orders onto the 1024×520 CCD, spanning $\sim 5100 \text{ \AA}$ to $\sim 9000 \text{ \AA}$. The entrance aperture is a $1'' \times 10''$ slit and the resolution is nearly constant over the full wavelength range at $R \sim 3300$ with a native dispersion of $\sim 0.6 \text{ \AA pixel}^{-1}$. Both runs had typical seeing of $\sim 1''$, but were affected by clouds and thus varying transparency.

Compared to MagE, the Red Channel Echellette mode is less stable, and significant flexure affects exposures taken at different sky positions. In addition, observations were sometimes combined with longslit mode programs, necessitating reconfiguration of the echellette grating. Wavelength calibration is provided by HeNeAr arcs taken immediately after the science exposures and is accurate to $< 0.2 \text{ \AA}$ (gen-

erally better than 0.1 \AA). On the other hand, typically only 1-2 quartz lamp exposures were obtained after the science exposures, and the nighttime images are not well aligned with the daytime flats. We thus combined all flats for each observing run into a single master flat and trimmed orders in individual images to match the coverage in the master flat. Target acquisition relied on offsets from nearby bright stars; we also obtained brief spectra of the acquisition stars prior to applying the offset in order to aid with object tracing. Finally, flux calibration was obtained from observations of a single standard star each night.

The MMT spectra were processed with similar procedures as MASE using custom-built routines implemented in Python. Bias subtraction was performed first using a low-order polynomial fit to the overscan region, and then a second-order correction from a median-combined bias image. The master pixel flats were then applied, and cosmic rays were identified and masked as outliers in groups of im-

ages obtained for the same target in succession. A simple median along image columns was used for sky subtraction as the slit axis is well aligned with the image columns. Spectra of the acquisition reference stars were used to obtain the slit profiles of the objects. These profiles were then used for optimal extraction (Horne 1986) of the 2D spectra. The extracted spectra were then flux calibrated, and the individual order spectra were then projected onto a common logarithmic wavelength grid and combined using inverse-variance weighting (again excluding the object contribution to the variance). As with the Magellan observations, nightly observations were processed independently and then combined to produce final spectra for each object, which are presented in Figure 1.

2.3 VLT spectra

The X-shooter instrument (Vernet et al. 2011) on the VLT 8m Kueyen telescope was used to obtain spectra of 4 quasars at $z \sim 6$ as part of a GTO program (P.I. V. D’Odorico) carried out between 2010 January and 2011 June. The spectra of three more quasars at $z \sim 6$ observed at comparable signal-to-noise ratio were downloaded from the X-shooter archive. The three arms of X-shooter allow for complete wavelength coverage between 3000 Å and 2.5 μm. The Ly α and Ly β forests of the observed objects fall in the VIS arm, which spans the region between 5500 Å and 10300 Å, approximately. The observations were carried out with a slit of width 0'7 for J0836+0054, J1306+0356, J1319+0950, and J0148+0600; and of width 0'9 for J0818+1722, J1030+0524 and J1509-1749; corresponding to resolutions $R \sim 11000$ and $R \sim 8800$, respectively. The raw spectra were reduced using the dedicated ESO pipeline (Modigliani et al. 2010) until the science spectrum extraction step (see below). A detailed description of the data reduction and the analysis of metal absorption systems in six of the quasar spectra can be found in D’Odorico et al. (2013).

We found the pipeline-reduced X-shooter spectra had small positive residuals in the dark portions of the spectra. This may be due to underestimation of the mean sky level, or the method of combining spectra (see §2.1). These residuals rose to the level of $\gtrsim +0.2\sigma$ in some cases. While this would not affect most analyses, our dark pixel statistic is extremely sensitive to the pixel flux distribution in zero-flux regions. Starting with the fully processed 2D spectra (i.e., after sky subtraction and rectification), we re-extracted the 1D spectra using optimal extraction¹ (Horne 1986) and then combined the spectra without including the contribution from the object flux in the variance (White et al. 2003). In a few cases, we also fit a smoothly varying spline function to the sky pixels in the 2D spectra prior to extraction, in order to remove a small sky residual. After applying this post-processing, we found the pixel flux residuals after sky subtraction to be correctly distributed about zero for sky pixels. The reduced spectra of J1306+0356 and J1319+0950 are shown in Figure 1.

¹ The algorithm of (Horne 1986) includes the object contribution to the variance; when extracting our spectra – including the MMT and Magellan spectra – we remove this term to avoid the associated bias.

3 DARK PIXEL ANALYSIS

We derive constraints on the neutral hydrogen fraction using an analysis of dark pixels in the spectra of high redshift quasars. Dark pixels are defined by having zero measured flux; the motivation for using dark pixels as a constraint on \bar{x}_{HI} is given in Mesinger (2010). In brief, any physical region containing pre-reionization neutral hydrogen will result in completely saturated absorption in the resonant Lyman series transitions. Therefore the wavelength associated with that transition in the spectrum of a background quasar will have zero flux. Dark pixels may also result from collapsed, self-shielded systems (e.g., Damped Lyman-alpha absorbers, or DLAs) and from post-reionization ionized gas with sufficient optical depth to render the flux undetectable given the finite S/N limit of the spectrum. Thus the dark fraction (fraction of the pixels which are dark) provides only an upper limit on \bar{x}_{HI} . Nevertheless, this upper limit can be competitive with other estimates, is directly related to the volume filling factor of H I, and *is completely independent of astrophysics*. In contrast, the more common “effective optical depth” statistic, $\tau_{\text{GP}}^{\text{eff}} \equiv -\ln(\langle f_{\text{obs}}/f_{\text{cont}} \rangle_{\Delta z})$, is highly sensitive to: (i) transmission in rare voids (which is both difficult to simulate and not directly related to \bar{x}_{HI}), and (ii) the estimate of the intrinsic quasar continuum, f_{cont} (e.g., Lee 2012).

In general we follow the same procedures outlined in Paper I to analyze the dark pixel fractions in our spectra, and we refer the reader to that work for further details. For completeness we provide a brief summary of the methodology here, and discuss small changes to the analysis adopted for this work.

First, for the purposes of our analysis, we use the term “pixel” to refer to a 3.3 comoving Mpc region obtained by binning the individual spectral pixels. Binning the data increases the dynamic range and thus strengthens our constraints, while the binned pixel size is chosen to retain information on physical structures at scales we are interested in (see Paper I for a more detailed justification of this choice). As we now have several instances of multiple spectra of the same quasar obtained from different telescope/instrument combinations, we combine the spectra at the stage of computing the binned pixels using inverse-variance weighting of the individual contributions. The dark pixel fractions are then calculated in wide redshift bins ($\Delta z \sim 0.2$) from the binned pixels. One modification to our analysis from Paper I is that we select the redshift bins for the Ly α and Ly β forests to avoid wavelengths associated with regions of strong telluric absorption.

In Paper I we explored two methods for counting dark pixels in real (i.e., noisy) spectra. The first counted all pixels with $< 2\sigma$ flux based on the rms noise estimate in the spectrum, then scaled this number by the small fraction of zero flux pixels expected to scatter above this threshold (2.3% assuming Gaussian statistics). The second method counted all pixels with a measured flux < 0 ; in this case the scaling factor is two, as dark pixels are equally likely to have negative or positive values if the noise is symmetric around zero. The advantage of the first method is reduced uncertainties as more pixels contribute to the statistic. However, this method directly relies on the per-pixel noise estimate and thus a complete and precise accounting for all variance

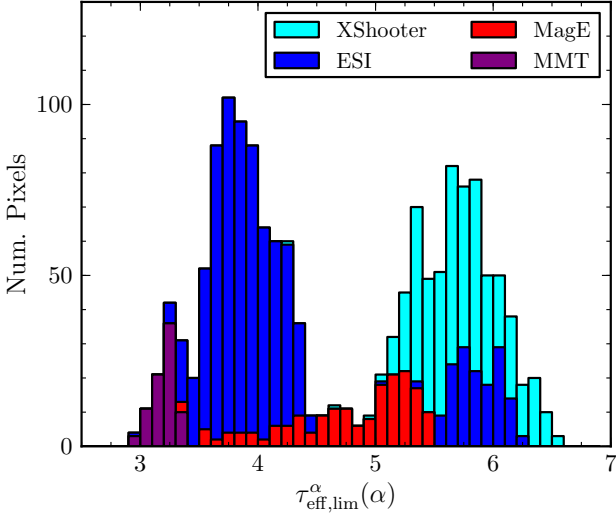


Figure 2. Depth of the Ly α pixels for the full dataset, quantified by the 1σ limiting effective optical depth in a bin of 3.3 cMpc (see text for details). The distribution for the Ly β pixels is highly similar, although the numbers are smaller due to the shorter extent of the Ly β forest. The ESI spectra used in Paper I were mainly shallow spectra with $\tau \lesssim 4$. This work represents a substantial increase in the number of pixels that probe depths of $\tau_{\text{eff,lim}}^{\alpha} > 4.5$. The pixels have been color-coded by the source of the spectrum; where multiple instruments were used the deeper spectrum is adopted (for example, two of the objects observed with MMT also have VLT observations).

terms. On the other hand, the negative pixel counts require only that the mean of the noise is zero and that the noise is symmetrically distributed about this value.

As a simple test of the pixel flux statistics for spectral regions without any object flux, we examine the distribution of pixel fluxes for pixels blueward of the Lyman Limit for each quasar spectrum. This region should be completely dark for $z \sim 6$ quasars due to the high incidence of Lyman Limit Systems (LLSs), and thus can be used to quantify any sky subtraction residuals. We find that the pixels in our final processed spectra are indeed symmetrically distributed about zero flux in the Lyman Limit region, although the noise estimates in our heterogeneous dataset do not always strictly follow Gaussian statistics². We thus adopt only the negative pixel method in this work.

We use the metal line identifications compiled by D’Odorico et al. (2013) and Becker et al. (2011) to mask wavelengths associated with strong absorption systems. D’Odorico et al. (2013) provide a catalog of absorption systems associated with the high-ionization C IV transition, while the Becker et al. (2011) catalog includes low-ionization systems, namely O I, C II, and Si II. Although the actual amount of H I absorption is unconstrained, we simply mask pixels at the Lyman series wavelengths associated with the metal line redshifts for all systems with $\text{EW} > 0.3 \text{ \AA}$. This includes masking Ly α absorption within the Ly β forest, as

any DLA at these wavelengths would masquerade as Ly β dark pixels. In practice, few such systems fall within our redshift bins (as expected from the incidence of DLAs at these redshifts, e.g., Songaila & Cowie 2010), so this has little effect on our final results.

We quantify the depth of each pixel in the same manner as Paper I by calculating a 1σ limit to the effective optical depth as $\tau_{\text{lim}}^{\text{eff}} = -\ln((\sigma/f_{\text{cont}}))$, where σ is the noise estimate for the binned pixels in the combined spectra, and f_{cont} is the estimated continuum flux at the wavelength associated with the pixel³. The continuum fit uses the broken power-law UV continuum model of Shull et al. (2012), normalized to the flux at 1350 \AA . Table 1 lists the median limiting effective optical depths in the Ly α forests of each spectrum. We stress that these values merely serve to quantify the data quality, and are not used in deriving our results.

We use the same wavelength ranges for the Ly α and Ly β forests: starting at $1 + z_{\text{min}}^{\alpha} = (1 + z_{\text{em}})(1040\text{\AA}/\lambda_{\alpha})$ and $1 + z_{\text{min}}^{\beta} = (1 + z_{\text{em}})(970\text{\AA}/\lambda_{\beta})$, respectively, and ending at $z_{\text{QSO}} - 0.1$ to avoid bias from the local quasar overdensity. We calculate dark pixel fractions independently in the two forests, and then in the combined Ly α +Ly β forest by aligning the pixels in absorption redshift and then counting pixels that have negative flux in both forests. For the individual forests, the fraction of negative pixels are multiplied by two to obtain the \bar{x}_{HI} constraint; this factor accounts for the additional pixels which intrinsically have zero flux, but are recorded to have positive values due to the noise. Likewise, the fraction of pixels with recorded negative values in *both* Ly α and Ly β are scaled by a factor of four to obtain \bar{x}_{HI} limits. Again, this analysis assumes only a symmetric distribution around zero for zero-flux pixels. Finally, the uncertainties on the dark pixel fractions are calculated using the same jackknife method as described in Paper I; briefly, we account for sightline variance by computing the dark fractions in subsamples removing one quasar at a time, then use the resulting jackknife estimates of the mean and standard deviation from the subsamples for our analysis.

4 RESULTS

The new, deeper spectra presented here result in a significant improvement to our results from Paper I, in that many pixels that would previously have been classified as “dark” are now detected in the higher S/N spectra. These pixels sample regions of the IGM with large optical depths ($4 \lesssim \tau_{\text{eff}}^{\alpha} \lesssim 6$) but that are not associated with pre-reionization neutral regions. Figure 2 displays a histogram of the limiting effective optical depths of the spectra analyzed here. The new spectra, in particular from X-shooter, provide a much larger sample of high- S/N pixels. Figure 3 compares our previous results directly, using the same cut on spectral quality ($\tau_{\text{eff,lim}}^{\alpha} > 2.5$). It is apparent that the much larger number of pixels greatly improves the statistics (as evident from the smaller error bars), but has little effect on the resulting dark pixel fractions (and hence \bar{x}_{HI} constraint).

On the other hand, if we apply a much more stringent

² The ESI spectra used in Paper I, reduced using the method described in White et al. (2003), do present highly Gaussian noise properties according to this test.

³ In Paper I we tabulated the 2σ limit, but since we are not using the 2σ threshold method to define dark pixels in this work we quote the 1σ limits.

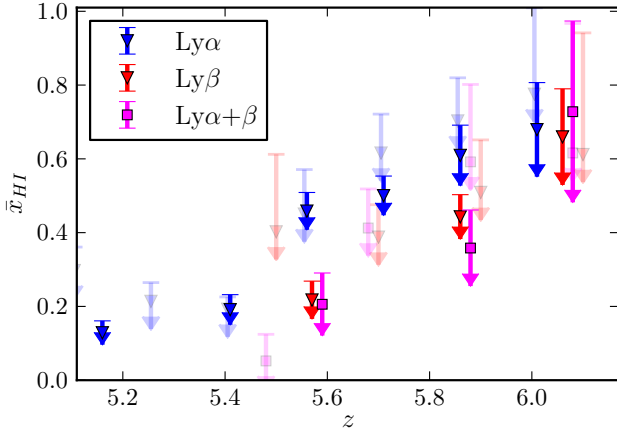


Figure 3. Comparison of the constraint on \bar{x}_{HI} obtained from the new data (dark points) to the data used in Paper I (light points). There are small differences in the placement of the redshift bins, and the $\text{Ly}\beta$ and $\text{Ly}\alpha+\text{Ly}\beta$ points are offset slightly for clarity. Including all of the data results in only a small improvement, although the error bars are considerably reduced due to the better statistics.

quality cut of $\tau_{\text{eff,lim}}^{\alpha} > 4.5$ using the new data, the resulting constraint is much stronger, as seen in Figure 4. This cut is chosen to reflect the bimodal distribution in τ seen in Fig. 2, roughly dividing the spectra at one hour of integration time. Applying this cut removes noisy pixels with insufficient sensitivity to probe the large optical depth regions of the IGM. In Paper I, the deep sample consisted of only two sightlines and was thus subject to cosmic variance, whereas now each bin – even in the combined $\text{Ly}\alpha+\text{Ly}\beta$ forest with relatively small overlap – contains at least four objects. We tabulate the dark pixel fractions, which translate directly into the \bar{x}_{HI} constraint, in Table 2.

Introducing a quality cut using the effective optical depth measurements does tie our results to the continuum estimates, however, only very weakly. First, continuum errors on the order of 20–30% will have little effect on the pixel distribution in our analysis (see Fig. 2). Second, as the quasar continuum shape is uncorrelated with the absorption properties of the forest, continuum errors will cause pixels to move above or below the quality cut in an unbiased fashion. It is important to stress that the quality cut only affects the selection of pixels to be included in the analysis, the designation of dark pixels does not make use of the continuum estimate.

We find a single pixel with negative flux in the combined $\text{Ly}\alpha+\text{Ly}\beta$ forests in each of the $z \approx 5.6$ and $z \approx 5.9$ redshift bins. As explained above, this translates to an expectation of ~ 4 dark patches in each redshift bin, with the resulting 1σ jackknife limits of $\bar{x}_{\text{HI}} < 0.11$ (0.09) at $z \approx 5.9$ (5.6). These limits are a factor of 2–3 improvement over the ones in Paper I, in which we were unable to conclude that reionization had completed by $z \sim 5$. With the available S/N and an effective sightline length of ~ 300 Mpc in each redshift bin, we expect \sim few dark patches just from a post-reionization IGM (e.g. Fig. 6 in Mesinger 2010). Our results at $z < 6$ are therefore fully consistent with a post-overlap IGM.

Our limits of $\bar{x}_{\text{HI}} < 0.11$ (0.09) at $z \approx 5.9$ (5.6) are the

Table 2. Upper limits on \bar{x}_{HI} obtained from the high S/N sample ($\tau_{\text{eff,lim}}^{\alpha} > 4.5$)

| z_1 | z_2 | N_{LOS} | N_{pix} | f_{dark} | $+1\sigma$ |
|--------------------------------|-------|------------------|------------------|-------------------|------------|
| Ly α forest | | | | | |
| 5.085 | 5.235 | 8 | 148 | 0.08 | 0.06 |
| 5.335 | 5.485 | 10 | 139 | 0.09 | 0.02 |
| 5.485 | 5.635 | 10 | 160 | 0.24 | 0.08 |
| 5.635 | 5.785 | 9 | 140 | 0.21 | 0.10 |
| 5.785 | 5.935 | 7 | 72 | 0.42 | 0.13 |
| 5.935 | 6.085 | 4 | 51 | 0.47 | 0.15 |
| Ly β forest | | | | | |
| 5.480 | 5.680 | 6 | 104 | 0.13 | 0.06 |
| 5.770 | 5.970 | 6 | 96 | 0.23 | 0.11 |
| 5.970 | 6.170 | 4 | 50 | 0.44 | 0.18 |
| Ly α +Ly β forest | | | | | |
| 5.480 | 5.680 | 6 | 92 | 0.04 | 0.05 |
| 5.770 | 5.970 | 6 | 76 | 0.06 | 0.05 |
| 5.970 | 6.170 | 4 | 60 | 0.38 | 0.20 |

Notes: The first two columns give the redshift ranges in which the dark pixel fractions are calculated. The third column is the number of lines-of-sight contributing to the redshift bin, and the fourth column is the number of pixels in that bin. The fifth column is the dark pixel fraction (scaled from the negative pixel counts), and the final column is the 1σ uncertainty on this fraction from jackknife statistics.

most robust evidence to date that reionization has completed by $z \approx 6$. In the context of simple patchy reionization models, this new limit on the end to reionization is even more stringent than provided by the CMB Thompson scattering optical depth (e.g. Mesinger et al. 2012).

Our sample includes the quasar J0148+0600, which was reported by Becker et al. (2014) to have a complete Gunn-Peterson trough in the $\text{Ly}\alpha$ forest extending from $5.523 \leq z \leq 5.879$. Indeed, this quasar significantly increases the dark pixel fractions in the $\text{Ly}\alpha$ forest at $z < 6$. However, there are multiple transmission spikes in the $\text{Ly}\beta$ forest. In fact, the aligned $\text{Ly}\alpha$ and $\text{Ly}\beta$ forests *have only a single pixel with negative flux in both forests* (corresponding to the value of four expected dark patches quoted in the above results for this redshift bin). The fact that the $\text{Ly}\alpha$ forest is dark and yet the $\text{Ly}\beta$ is not, implies that for a large part of the sightline the $\text{Ly}\alpha$ optical depth is $6 \lesssim \tau_{\text{eff}}^{\alpha} \lesssim 10$. This is inconsistent with pre-overlap neutral patches (with $\tau \sim 10^5$). Instead, this sightline demonstrates the presence of large-scale fluctuations in the photo-ionizing background at these redshifts (Becker et al. 2014), consistent with theoretical expectations (e.g. Crociani et al. 2011).

Finally, our highest redshift bin does not show improvement compared to the Paper I results, with $\bar{x}_{\text{HI}} < 0.58$ at $z = 6.1$ (1σ). We now have twice as many sightlines contributing to this bin and thus employ the jackknife method to estimate the uncertainty (compared to Paper I where we estimated the cosmic variance expected from only two sightlines using models of patchy reionization).⁴ However, there is little gain in depth, as the limiting $\tau_{\text{eff}}^{\alpha}$ for the new data

⁴ Our 4-6 sightlines are able to sample the cosmic variance from patchy reionization to better than 1σ for $\bar{x}_{\text{HI}} \sim 0.1$ (see Fig. 6

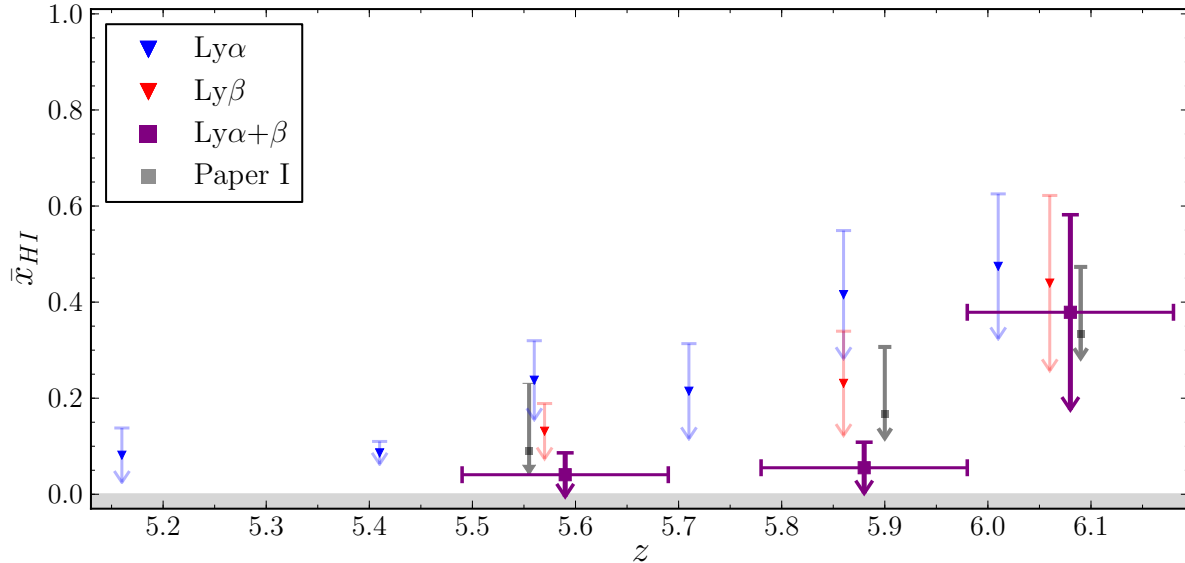


Figure 4. Constraint on the neutral hydrogen fraction from the best sample of spectra ($\tau_{\text{eff,lim}}^{\alpha} > 4.5$). The individual Ly α and Ly β constraints are shown in light blue and light red, respectively, with vertical error bars representing the sightline-to-sightline scatter in the dark fractions estimated from jackknife statistics. The strongest constraints are obtained by combining information from the Ly α and Ly β forests, denoted by the dark purple points, with horizontal error bars indicating the extent of the redshift bins. The grey upper limits are from the two Keck ESI spectra presented in Paper I (1σ limits); the $z \sim 6.1$ constraint is not improved due to the lack of bright quasars at $z > 6.2$, but now has model-independent error bars (see text for details). The constraints at $z < 6$ are considerably stronger, with $\bar{x}_{\text{HI}}(z) = 5.87 < 0.11$ and $\bar{x}_{\text{HI}}(z) = 5.58 < 0.09$ (both 1σ).

is similar to that of the two deepest Keck spectra in Paper I. Thus the resulting constraint on \bar{x}_{HI} is not improved, with the the now model-independent error bars resulting in 1σ constraints somewhat weaker than our previous estimate from two spectra. Further improvement in this redshift bin is limited by the lack of bright quasars with known redshifts greater than six; in addition, the Ly α forest is increasingly filled with strong night sky emission lines at wavelengths corresponding to this redshift, resulting in highly noisy spectra.

5 SUMMARY

We have updated our constraints on the neutral hydrogen fraction at $z \sim 5-6$ using a sample of 20 high-S/N quasar spectra obtained with Magellan, MMT, and the VLT (complementing our previous work with Keck spectra). Using a simple, model-independent statistic — the dark pixel fraction — we obtain new 1σ upper limits of $\bar{x}_{\text{HI}} < 0.11$ (0.09) at $z = 5.9$ (5.5). The dark pixel statistic unambiguously demonstrates that reionization is highly complete by $z \lesssim 6$. Our model-independent constraints can be used to confront theoretical models of inhomogeneous reionization.

Substantially improving on these new constraints would require an order of magnitude improvement in the statistics. Although Pan-STARRS is now delivering large samples of newly discovered bright quasars at $z \sim 6$ (Bañados et al. 2014), this is not likely enough to obtain a $< 1\%$ constraint on \bar{x}_{HI} using dark pixel statistics. Therefore, we expect little observational improvements on our results.

in Paper I). We therefore consider our current sample size large enough to justify the use of jackknife statistics.

On the other hand, the constraints on \bar{x}_{HI} can be improved by theoretical modeling of IGM properties and inhomogeneous reionization. Although by necessity this would involve model-dependencies, exploring a reasonably constrained set of IGM parameters would still yield reliable results that are consistent with the model-independent upper limits presented here. We leave this to a future work.

Acknowledgements

We thank the referee for a careful read of the manuscript and suggestions that improved the clarity of the text. IDM acknowledges support from NSF grants AST 08-06861 and AST 11-07682. Based in part on observations collected at the European Southern Observatory Very Large Telescope, Cerro Paranal, Chile – Programs 084.A-0390, 084.A-0550, 085.A-0299, 086.A-0162, 087.A-0607 and 268.A-5767. This paper also includes data obtained with the MMT Observatory, a joint facility of the University of Arizona and the Smithsonian Institution, and with the 6.5-m Magellan Telescopes located at Las Campanas Observatory, Chile. The authors wish to recognize and acknowledge the very significant cultural role and reverence that the summit of Mauna Kea has always had within the indigenous Hawaiian community. We are most fortunate to have the opportunity to conduct observations from this mountain.

Facilities: Keck:II (ESI), MMT (Red Channel spectrograph), Magellan:Clay (MagE), VLT:Kueyen (X-shooter)

REFERENCES

Bañados E., Venemans B. P., Morganson E., et al., 2014,

- AJ, 148, 14
- Becker G. D., Bolton J. S., Madau P., Pettini M., Ryan-Weber E. V., Venemans B. P., 2014, ArXiv e-prints
- Becker G. D., Sargent W. L. W., Rauch M., Carswell R. F., 2011, ApJ, 744, 91
- Bochanski J. J., Hennawi J. F., Simcoe R. A., et al., 2009, PASP, 121, 1409
- Bolton J. S., Haehnelt M. G., 2007, MNRAS, 374, 493
- Bolton J. S., Haehnelt M. G., Warren S. J., Hewett P. C., Mortlock D. J., Venemans B. P., McMahon R. G., Simpson C., 2011, MNRAS, 416, L70
- Carilli C. L., et al., 2010, ApJ, 714, 834
- Crociani D., Mesinger A., Moscardini L., Furlanetto S., 2011, MNRAS, 411, 289
- Croft R. A. C., 1998, in A. V. Olinto, J. A. Frieman, & D. N. Schramm ed., Eighteenth Texas Symposium on Relativistic Astrophysics Characterization of Lyman Alpha Spectra and Predictions of Structure Formation Models: A Flux Statistics Approach. pp 664+
- Dayal P., Maselli A., Ferrara A., 2011, MNRAS, 410, 830
- Dijkstra M., Mesinger A., Wyithe J. S. B., 2011, MNRAS, 414, 2139
- D’Odorico V., Cupani G., Cristiani S., et al., 2013, arXiv
- Fan X., Narayanan V. K., Lupton R. H., et al., 2001, AJ, 122, 2833
- Fan X., Strauss M. A., Becker R. H., et al., 2006, AJ, 132, 117
- Furlanetto S. R., Zaldarriaga M., Hernquist L., 2004, ApJ, 613, 1
- Gallerani S., Choudhury T. R., Ferrara A., 2006, MNRAS, 370, 1401
- Gallerani S., Ferrara A., Fan X., Choudhury T. R., 2008, MNRAS, 386, 359
- Hinshaw G., et al., 2013, ApJS, 208, 19
- Horne K., 1986, PASP, 98, 609
- Jensen H., Laursen P., Mellema G., Iliev I. T., Sommer-Larsen J., Shapiro P. R., 2013, MNRAS, 428, 1366
- Kashikawa N., et al., 2006, ApJ, 648, 7
- Komatsu E., Dunkley J., Nolte M. R., et al., 2009, ApJS, 180, 330
- Konno A., et al., 2014, ArXiv e-prints
- Lee K.-G., 2012, ApJ, 753, 136
- Lidz A., McQuinn M., Zaldarriaga M., Hernquist L., Dutta S., 2007, ApJ, 670, 39
- McGreer I. D., Mesinger A., Fan X., 2011, MNRAS, p. 1096
- Malhotra S., Rhoads J. E., 2004, ApJ, 617, L5
- Marshall J. L., Burles S., Thompson I. B., et al., 2008, in Ground-based and Airborne Instrumentation for Astronomy II Proceedings of SPIE. SPIE, pp 701454–701454–10
- Maselli A., Gallerani S., Ferrara A., Choudhury T. R., 2007, MNRAS, 376, L34
- McQuinn M., Hernquist L., Zaldarriaga M., Dutta S., 2007, MNRAS, 381, 75
- McQuinn M., Lidz A., Zaldarriaga M., Hernquist L., Dutta S., 2008, MNRAS, 388, 1101
- Mesinger A., 2010, MNRAS, 407, 1328
- Mesinger A., Aykutalp A., Vanzella E., Pentericci L., Ferrara A., Dijkstra M., 2014, ArXiv e-prints:1406.6373
- Mesinger A., Haiman Z., 2004, ApJ, 611, L69
- Mesinger A., Haiman Z., 2007, ApJ, 660, 923
- Mesinger A., McQuinn M., Spergel D. N., 2012, MNRAS, 422, 1403
- Modigliani A., Goldoni P., Royer F., et al., 2010, in Silva D. R., Peck A. B., Soifer B. T., eds, SPIE Astronomical Telescopes and Instrumentation: Observational Frontiers of Astronomy for the New Decade The X-shooter pipeline. SPIE, pp 773728–773728–12
- Schroeder J., Mesinger A., Haiman Z., 2012, MNRAS, 428, 3058
- Shull J. M., Stevans M., Danforth C. W., 2012, ApJ, 752, 162
- Songaila A., Cowie L. L., 2002, AJ, 123, 2183
- Songaila A., Cowie L. L., 2010, ApJ, 721, 1448
- Totani T., Aoki K., Hattori T., et al., 2013, arXiv:1312.3934v1
- Totani T., Kawai N., Kosugi G., Aoki K., Yamada T., Iye M., Ohta K., Hattori T., 2006, PASJ, 58, 485
- Vernet J., Dekker H., D’Odorico S., et al., 2011, A & A, 536, 105
- White R. L., Becker R. H., Fan X., Strauss M. A., 2003, AJ, 126, 1
- Wyithe J. S. B., Loeb A., Carilli C., 2005, ApJ, 628, 575
- Zahn O., et al., 2012, ApJ, 756, 65
- Zahn O., Mesinger A., McQuinn M., Trac H., Cen R., Hernquist L. E., 2011, MNRAS, 414, 727